Ocean Engineering 59 (2013) 73–85

Contents lists available at SciVerse ScienceDirect

Ocean Engineering

journal homepage: www.elsevier.com/locate/oceaneng

Fully nonlinear viscous wave generation in numerical wave tanks

M. Anbarsooz *, M. Passandideh-Fard, M. Moghiman

Mechanical Engineering Department, Ferdowsi University of Mashhad, Mashhad 9177948944, Iran

ARTICLE INFO

Article history:
Received 22 May 2012
Accepted 25 November 2012

Keywords:
Numerical wave tank
Viscous wave generation
Flap-type wavemaker
Piston-type wavemaker
Solitary wave

ABSTRACT

A numerical method for simulating the complete physics of the fully nonlinear viscous wave generation phenomenon is presented. To accomplish this objective, the motion of a solid body representing the wave generating mechanism is modeled. In this paper, both the piston-type and flap-type wavemakers are simulated and the results of the model are compared with those of the experiments and analytics. The unsteady, two dimensional Navier–Stokes equations are solved in conjunction with the volume-of-fluid method for treating the free surface. A wide range of waves from linear to nonlinear generated by piston and flap-type wavemakers in intermediate and deep water cases are studied in this paper. The accuracy of the numerical results is verified by a comparison with the results of the wavemaker theory, the available experimental data in the literature, and the experiments preformed in this study. For the cases with small wave steepness, the numerical results agree well with the theoretical and experimental results for both the piston and flap-type wavemakers. However, for cases with large wave steepness, the numerical and experimental wave heights are slightly lower than the analytics. In both the piston and flap-type wavemakers, the numerical results are in good agreement with the measurements.

1. Introduction

Studying water wave impacts on costal structures and various related coastal phenomena are often performed in physical wave tanks and flumes, where a paddle with prescribed motion produces the desired waves. A numerical wave tank is an alternative to the physical modeling because studying different wave conditions and implementing the modifications are more conveniently performed using numerical models. However, there exist some difficulties in wave-making problems using numerical models. These difficulties include moving boundaries at the free surface, wavemaker boundary conditions, and the selection of appropriate nonreflecting far-field boundary conditions. In the literature, three different approaches have been reported for wave-making problems: analytical models, numerical models assuming an inviscid fluid, and numerical models considering a viscous fluid. What follows is a review of these models and the corresponding studies.

Assuming an inviscid flow, analytical solutions for piston-type and flap-type wavemakers are derived using linear wave theory by Havelock (1929) and Hyun (1976). However, the experimental measurements of Ursell et al. (1960) for varying the wave steepness produced by a piston type wavemaker revealed that for a large wave steepness, the measured wave heights are typically 10% below the values predicted by the linear wave theory. Madsen (1971) extended classical linear wave theory to second-order accuracy in order to study the generation of long waves. The second-order theory was used by other researchers such as (Flick and Guza, 1980; Moubayed and Williams, 1993; Schäffer, 1996, etc.) and was developed to higher orders by Schwartz (1974). The second-order wave theory leads to an anomalous bump in the wave trough for large waves (Dean and Dalrymple, 1984). Therefore, higher order solutions were proposed such as third order by Borgman and Chappelear (1958) and fifth order by Fenton (1985). Expanding the wave theory to higher orders becomes extremely complicated. As a result, wave theories with higher orders are studied numerically. The need for numerical models also arises from the fact that studying surface waves in the presence of an arbitrary shaped solid object cannot be accomplished using analytical models of any order.

A numerical high-order wave theory for highly non-linear waves based on stream function wave theory was first introduced by Chappelear (1961) and further developed by (Dean,1965; Chaplin, 1979; Fenton, 1988; Zhang and Schäffer, 2007, etc.). Other numerical methods developed for generating waves are based on internal wave generation models. These models have the advantage of avoiding the interference with the boundary conditions. Larsen and Dancy (1983) were the first to use the source line method with the Boussinesq equations to make short waves. Several researchers developed this approach to generate linear

* Corresponding author. Tel.: +98511 8763304; fax: +98511 8626541.
E-mail address: m.anbarsooz@gmail.com (M. Anbarsooz).

0029-8018/$ - see front matter © 2012 Elsevier Ltd. All rights reserved.
http://dx.doi.org/10.1016/j.oceaneng.2012.11.011

Nomenclature

a	wave amplitude
c	wave celerity
d	still water depth
$\vec{F}_b$	body forces
f	liquid volume fraction
H	wave height $=2a$
Hc	height of the computational domain
k	wave number
L	wave length
Lc	length of the computational domain
$Ld1$, $Ld2$	length of the damping zones
p	pressure
S	stroke
t	time
Ur	Ursell number
$\vec{V}$	velocity vector
τ	duration of motion
x	horizontal coordinate distance
y	vertical coordinate distance
μ	dynamic viscosity
ρ	density
$\vec{\tau}$	stress tensor
φ_s	solid volume fraction
$\xi(t)$	piston trajectory
η	free surface elevation
$\Delta\theta$	angular span of the flapper motion

and non-linear waves for regular waves, irregular waves and multidirectional waves (Brorsen and Larsen, 1987; Li et al., 1999; Wei et al., 1999; Liu et al., 2005, etc.).

The inviscid fluid and irrotational flow assumptions used in the above-mentioned studies are not acceptable in many practical applications. Therefore, using numerical models with viscous fluid assumptions is inevitable. Chan and Street (1970) used a modified version of the so called marker and cell (MAC) method introduced by Harlow and Welch (1965) for free-surface flows to study the propagation of a solitary wave in a shallow channel. In the modified version, called the Stanford University modified MAC (SUMMAC), a more accurate technique was used to determine the velocity components at the surface cells. Tang et al. (1990) applied a more accurate mathematical expression for the dynamic boundary conditions on a free surface that included the viscosity and surface tension effects. The SUMMAC method along with exact free surface boundary conditions was also used by Huang et al. (1998) to investigate the nonlinear viscous wavefields generated by a piston-type wavemaker. The numerical scheme developed by Huang et al. (1998) was employed by Huang and Dong (2001) and Dong and Huang (2004) to generate different incident waves, including small- and finite-amplitude waves and solitary waves in a two dimensional wave flume. The same method was applied by Wang et al. (2007) for simulating a three dimensional numerical viscous wave tank equipped with a piston type wavemaker.

In 1981, Hirt and Nichols (1981) introduced the volume of fluid (VOF) method for treating the flows with a free surface. Since then many numerical wave tanks have been developed based on this method. The literature on the use of the VOF method for wave generation can be classified under two main categories. In the first category named here VOF-inflow method, the inflow boundary conditions are set based on the free surface elevation and the velocity components obtained from analytical solution of the desired wave. Lin and Liu (1998) were first to use this technique for wave generation in a two dimensional wave flume. This method was also used by Troch and De Rouck (1999) to develop an active wave generating-absorbing boundary condition. They also provided an overview of the development of the VOF type models with more attention to coastal engineering applications. However, Li and Fleming (2001) and Apsley and Hu (2003) developed a three dimensional viscous wave flume using the VOF-inflow technique. The wave generation using this method was also used by several researchers (Huang and Dong, 2001; Karim et al., 2009; Park et al., 2003; Shen and Chan, 2008; Suea et al., 2005; Zhao et al., 2010a, etc.) in various coastal applications.

The second category of the VOF based models for the wave generation is the so called internal wave generation method in which a mass source function is introduced in a certain region inside the computational domain (Lin and Liu, 1999). In this method, the fluid is alternatively injected or sucked into this region such that it produces the same physical effect as of the desired wave. Various types of waves including linear monochromatic; irregular; the Stokes second and higher orders; solitary; and cnoidal can be generated using this method through the proper definition of the source function (Lin and Liu, 1999). This model has been successfully used by Kawasaki (1999) to study wave breaking over submerged breakwater, by Hieu and Tanimoto (2006) to simulate wave–structure interactions, and by Hur and Mizutani (2003) and Hur et al. (2004) to determine the transverse wave forces that act on 3D asymmetric structures on a submerged permeable breakwater. A modification of this method was introduced by Hafsia et al. (2009) whose work resulted in the reduction of the source domain to a one-dimensional region.

Although the two above mentioned categories are capable of producing a desired free surface profile artificially, they are different from the real physical wave generation phenomenon. In the first category, the velocity components at the inflow boundary are set according to an analytical solution of the desired wave. Therefore, the velocity profile at this boundary is a function of vertical direction, while for example a piston-type wavemaker moves horizontally with a velocity that has no vertical variation. Similarly in the internal wave generation method, the added mass source term is computed according to a prescribed free surface profile. Clearly the flow pattern close to the source region is different from the flow pattern around a real physical wave generator paddle.

On the other hand, in a real wave generation mechanism, the resultant wave length is a function of the wavemaker period, stroke and the still water depth. Predicting the wavelength is performed using wavemaker theories. The linear wavemaker theory as completely presented by Dean and Dalrymple (1984) and the second order wavemaker theory as presented by Madsen (1971) are widely used for this purpose. However, in the wavemaker theories higher than the first order, if the wavelength is not known, either the wave speed or the mean velocity at a point in the fluid or the mass flux induced by the waves must be known, so that the wavelength can be obtained. If none of these are known, then application of the theory is irrational and likely to be in error at first order as stated by Fenton (1985). This is why for the steeper waves, the discrepancy between the experimental results and those of the wavemaker theory becomes more pronounced (Ursell et al., 1960).

Therefore, developing a numerical viscous wave tank which simulates the real physical process of wave generation is of great

interest. This goal can be accomplished by modeling the prescribed motion of the wave paddle inside the fluid. In this case, one only needs to specify the period and stroke of the wavemaker's motion in a water of specific depth; the wave length and wave height will be calculated through the complete solution of the Navier–Stokes equations. Wood et al. (2003) used the Fluent software for the piston-type wavemaker, and Finnegan and Goggins (2012) used the Ansys CFX commercial software for the flap-type wavemaker. In their Navier–Stokes solvers, the fluid–solid interaction is based on unstructured grids where solid zones are not considered in the computational domain and the object surfaces are treated as boundary conditions. As the solid body moves inside the fluid, the geometry of the fluid computational domain changes. Therefore, a re-meshing is inevitable in each time step or after a large distortion of the generated grid. The re-meshing is seen by most researchers as a process that should be avoided. As a result, this method has been rarely employed for wave generation as reviewed above. Furthermore, as Finnegan and Goggins (2012) pointed out, the wave generation in Ansys CFX using a flap-type wavemaker is restricted to a low normalized wavenumber.

In this study, a numerical method is presented which simulates the real physics of wave generation phenomenon. The numerical model employed for this purpose is the one developed by Mirzaii and Passandideh-Fard (2012) for modeling fluid flows containing a free surface in presence of an arbitrary moving object. The method is implemented in a VOF-based numerical program to accurately model the wave generation performed by piston and flap-type wavemakers. The presented model is capable of producing linear to strongly nonlinear waves in both the intermediate and deep water cases. The accuracy of the presented numerical model is verified by comparing the results of simulations with the analytical and experimental data. In the case of piston-type wavemaker, the experimental results of Ursell et al. (1960) are used, while in the case of flap-type wavemaker, the results of the experiments performed in this study are employed.

2. Governing equations and boundary conditions

The schematic of the wavemaker mechanisms considered in this study is given in Fig. 1 where both the piston and flap types are illustrated. The domain of the computation is a rectangle ($Lc \times Hc$) with two damping zones at both ends as shown in the figure. A solid object representing the wavemaker (piston or flap) is positioned at $x=Xp$ from the left and forced to move according to a prescribed harmonic motion. Both the linear motion of the piston-type wavemaker and the rotational motion of the flap-type wavemaker are simulated. What follows is a brief description of the model used for simulating the fluid flow and the solid object.

2.1. Fluid flow governing equations

The governing equations for fluid flow are the Navier–Stokes equations in 2D, Newtonian, incompressible and laminar flow:

$$\nabla \vec{V} = 0 \tag{1}$$

$$\frac{\partial V}{\partial t} + \vec{V} \cdot \nabla \vec{V} = -\frac{1}{\rho}\nabla p + \frac{1}{\rho}\nabla \cdot \vec{\tau} + \vec{g} + \frac{1}{\rho}\vec{F}_b \tag{2}$$

$$\vec{\tau} = \mu[\left(\nabla \vec{V}\right) + \left(\nabla \vec{V}\right)^T] \tag{3}$$

where $\vec{V}$ is the velocity vector, ρ the density, μ the dynamic viscosity, p the pressure, $\vec{\tau}$ the stress tensor and $\vec{F}_b$ represents body forces acting on the fluid. The interface is advected using the VOF method by means of a scalar field (f), the so-called liquid volume fraction, defined as:

$$f = \begin{cases} 0 & \text{in the gas phase} \\ 0 < , < 1 & \text{in the liquid-gas interface} \\ 1 & \text{in the liquid phase} \end{cases} \tag{4}$$

The discontinuity in f is a Lagrangian invariant, propagating according to:

$$\frac{df}{dt} = \frac{\partial f}{\partial t} + \vec{V} \cdot \nabla f = 0 \tag{5}$$

2.2. Solid object treatment

In this study, the wavemaker's paddle (piston-type or flap-type) is modeled as a solid object using the fast-fictitious-domain method (Sharma and Patankar, 2005) in which the solid is considered as a fluid with a high viscosity with a prescribed motion. In the first stage of a computation in each time step, the governing equations of fluid motion are solved everywhere in the

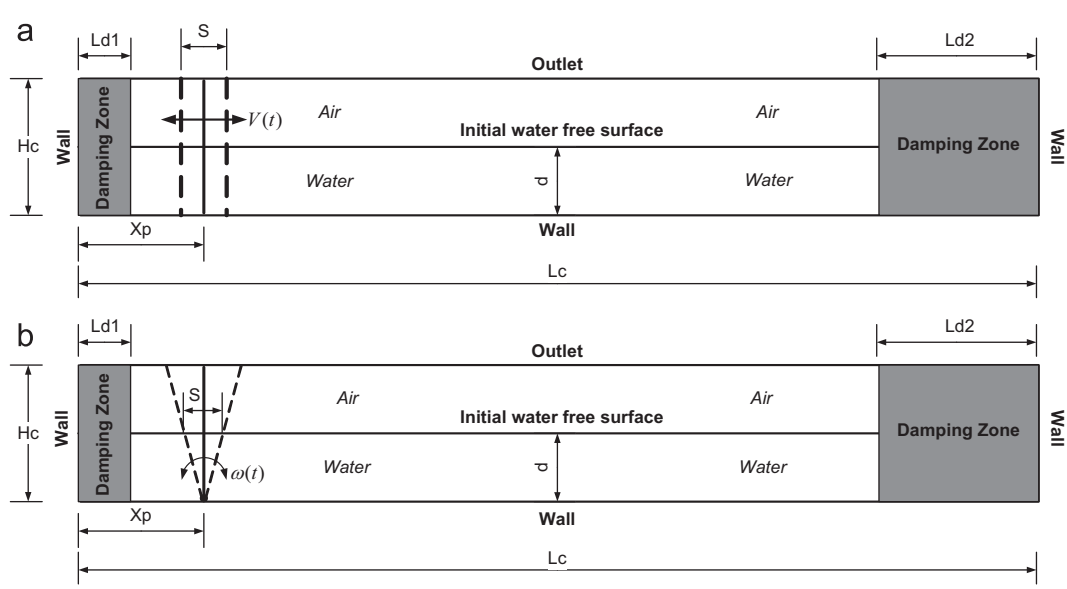

Fig. 1. Computational domain and boundary conditions for: (a) piston-type wavemaker; and (b) flap-type wavemaker.

computational domain including the paddle (solid zone) without any additional equation. Next, the paddle velocity is calculated (based on the pre-determined motion) and is imposed only within the solid zone; the change; however, is not projected into the fluid domain. Attributing an average velocity to the solid, leads to an unrealistic slip condition in the solid–liquid interface as stated by Sharma and Patankar (2005). In this study, therefore, we propose to correct the above drawback by attributing a high viscosity to the solid zone. A summary of the computational procedure followed in each time step of simulation is given below:

(1) The solid object in the computational domain is identified using a scalar parameter φ_s defined as:

$$\varphi_s = \begin{cases} 0 & \text{Out of the solid} \\ 0 < \ , \ < 1 & \text{Solid boundary} \\ 1 & \text{Within the solid} \end{cases} \tag{6}$$

(2) The fluid flow equations are solved everywhere in the computational domain including the solid zone as discussed above to obtain $\vec{V}^{n+1}$. In this step, the density and viscosity in each cell is defined as

$$\rho = f\rho_l + (1-f-\varphi_s)\rho_g + \varphi_s\rho_s \tag{7}$$

$$\mu = f\mu_l + (1-f-\varphi_s)\mu_g + \varphi_s\mu_s \tag{8}$$

where subscripts l, g and s refer to liquid, gas and solid, respectively. The viscosity of the solid is set by a large magnitude in comparison with that of the liquid. This large magnitude of viscosity implicitly imposes the no-slip condition on the solid–liquid interface. It has been shown by Mirzaii and Passandideh-Fard (2012) that using a viscosity two orders of magnitude larger than that of the fluid is large enough to have an accurate solid body movement. It should be noted that within the solid zone, the value of f is set to zero.

(3) The position and orientation of the solid object (piston or flap) are next calculated based on its prescribed motion and the corresponding velocity distribution inside the solid zone is updated accordingly. When the velocity in the computational domain is updated, the interface is advected using Eq. (5).

2.3. Initial and boundary conditions

The initial condition considered in this study is a still water with zero velocity and no surface waves. At the left, right and bottom boundaries of the computational domain as displayed in Fig. 1, the no slip condition for the velocity components is imposed. At the top of the domain, the outlet boundary with atmospheric pressure is used. For modeling the damping zone, wave absorption boundary conditions must be applied. The conditions set for this zone must be such that to allow running simulations for a long period of time, avoiding most of the effects of reflected waves. Lin and Liu (2004) introduced a friction source term in the momentum equation with an exponential damping law. Hafsia et al. (2009) employed the same concept but with a linear damping law used only in the vertical direction. In the present study, two passive absorption zones (see Fig. 1) are modeled in the simulations, one just behind the wavemaker and the other at the end of the computational domain. The method used for treating these regions is increased viscosity to a level high enough to effectively damp the energy of incident waves.

2.4. Numerical method

For the discretization of the governing equations, a three-step projection method is used in which the continuity and momentum equations are solved in three fractional steps (Mirzaii and Passandideh-Fard, 2012). In the first step, the convective and body force terms in the momentum equations are discretized using an explicit scheme. The viscosity and pressure terms in this step are not considered. An intermediate velocity field, $V^{n+1/3}$; is then obtained as:

$$\frac{\vec{V}^{n+1/3} - \vec{V}^{n}}{\delta t} = \left(-\vec{V}\nabla\cdot\vec{V}\right)^{n} + \frac{1}{\rho^n}\vec{F}_b^{\,n} \tag{9}$$

In this study, the no-slip condition on the solid–liquid interface is imposed by attributing a high viscosity to the solid region. As a result, the allowable time step for numerical simulation will decrease dramatically if the viscous term discretization is performed using an explicit scheme. This fact is due to a linear stability time step constraint for an explicit scheme (Harlow and Amsden, 1971). Therefore, in the second step, an implicit discretization scheme is used to model the viscous term of the momentum equation to obtain the intermediate velocity from this step, $V^{n+2/3}$ as:

$$\frac{\vec{V}^{n+2/3} - \vec{V}^{n+1/3}}{\delta t} = \frac{1}{\rho^n}\nabla\cdot\mu\left[\left(\nabla\vec{V}^{n+2/3}\right) + \left(\nabla\vec{V}^{n+2/3}\right)^T\right] \tag{10}$$

In this equation, the viscous term is discretized in the fractional time step $t^{n+2/3}$. This leads to an implicit treatment of the viscous term which, in turn, allows using a large time step for simulation of fluids with high viscosities. Eq. (10) is solved using a TDMA (Tri-Diagonal Matrix Algorithm) method to obtain $V^{n+2/3}$.

In the final step, the second intermediate velocity is projected to a divergence free velocity field as:

$$\frac{\vec{V}^{n+1} - \vec{V}^{n+2/3}}{\delta t} = -\frac{1}{\rho^n}\cdot\nabla p^{n+1} \tag{11}$$

The continuity equation is also satisfied for the velocity field at the new time step:

$$\nabla\cdot\vec{V}^{n+1} = 0 \tag{12}$$

Taking the divergence of Eq. (11) and substituting from Eq. (12) results in a pressure Poisson equation as:

$$\nabla\cdot\left[\frac{1}{\rho^n}\nabla p^{n+1}\right] = \frac{\nabla\cdot\vec{V}^{n+2/3}}{\delta t} \tag{13}$$

The obtained pressure field can then be used to find the final velocity field by applying Eq. (11). The resulting set of equations is symmetric and positive definite; a solution is obtained in each time step using an Incomplete Cholesky–Conjugate Gradient (LDLT) solver (Kershaw, 1978).

Eq. (5) is used to track the location of the interface and is solved according to the Youngs PLIC algorithm (Youngs, 1984). More details regarding the model and the free surface treatment are given elsewhere (Mirzaii and Passandideh-Fard, 2012).

3. Experimental setup

Various types of wavemakers have been reported in the literature to perform experiments in laboratories including piston, flap and plunger-type wavemakers. One of the most remarkable experiments ever reported in the literature is the one performed by Ursell et al. (1960) for small and large wave steepness using piston-type wavemaker, the results of which are used in this paper to validate the results of the numerical model. However, for the experimental setup in this study, a flap-type wavemaker is considered. The laboratory experiments were

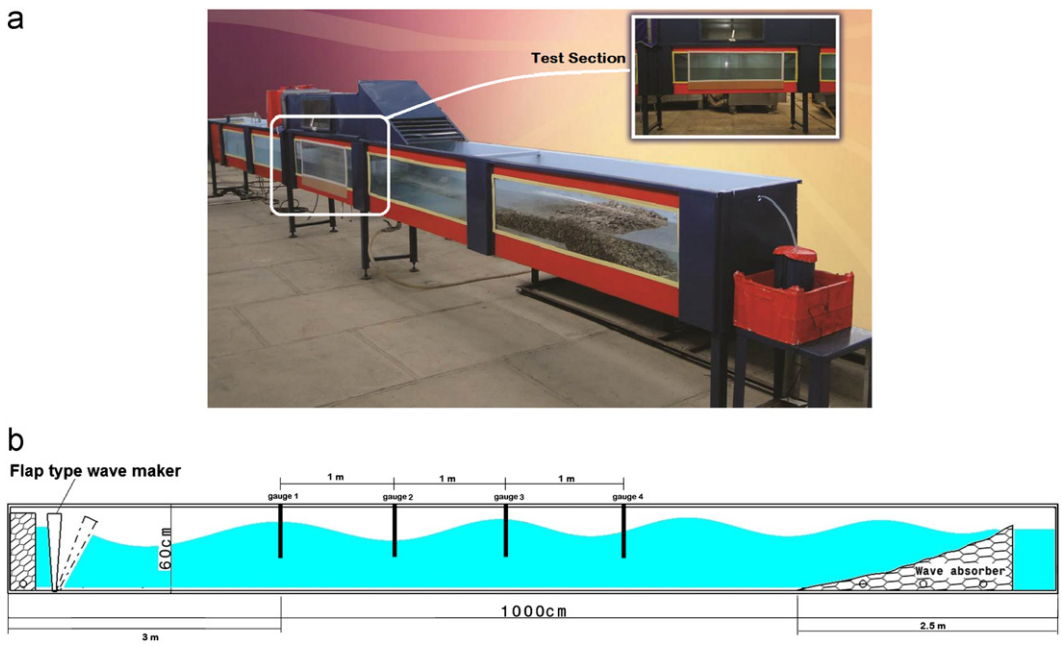

Fig. 2. A photograph (a) and a schematic (b) of the experimental setup. The drawing is not to scale.

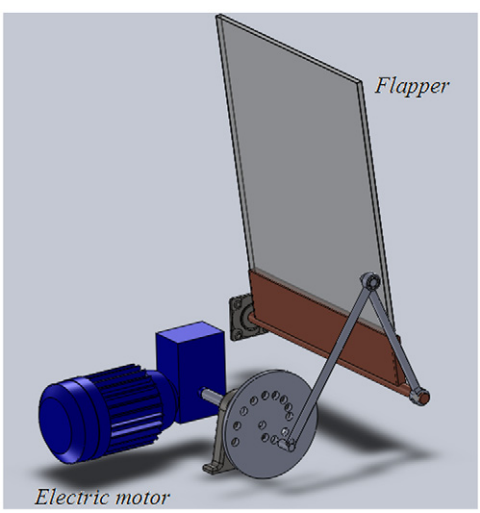

Fig. 3. Driving mechanism of the flap-type wavemaker.

conducted in a wave flume with a rectangular cross section at the Ferdowsi University of Mashhad. The flume is 10.0 m long, 0.5 m wide and 0.6 m high with two passive wave absorption zones at both ends. In order to investigate the effectiveness of the absorption zones, for all the experiments performed in this study, the reflection coefficient is determined. The incident wave is partially reflected from the absorption zone; the interference of the reflected wave and the incident wave results in a partial standing wave within the channel. Therefore, the resultant wave height is not the same at different locations along the channel; it rather oscillates about a mean value. The reflection coefficient ε_r of the absorption zone is defined as the ratio of the reflected wave height to the incident wave height. Ursell et al. (1960) recommended the following relation for ε_r:

$$\varepsilon_r = \frac{H_r}{H_i} = \frac{H_{\max} - H_{\min}}{H_{\max} + H_{\min}} \tag{14}$$

where H_{max} and H_{min} are the maximum and minimum values of the measured wave height along the channel. The reflection coefficient for all the experiments performed in this study was less than 10%. Since the wave heights are measured along nearly 4 meters of the channel, the wave attenuation is neglected.

A schematic of the experimental setup is shown in Fig. 2. The positions of the four capacitance wave probes are shown in this figure. Waves are generated by a flap-type wavemaker located at one side of the flume which is hinged at the bottom of the channel. Rubber seals are used to minimize the water leakage from the small clearance between the edges of the wavemaker plate and the side walls of the channel. The flap motion is generated using a four link mechanism with a controllable arm length coupled to an electric motor as shown in Fig. 3. By varying the arm length and the rotational speed of the electric motor, various flapper motion periods (0.8–3 s) and strokes can be produced.

4. Results and discussions

The ability of the proposed model to simulate various nonlinear wave generation phenomena is shown by generating a solitary wave using a piston-type wavemaker and 2nd order Stokes' progressive waves by piston and flap-type wavemakers.

4.1. Piston-type wavemaker – solitary wave

To validate the proposed generation method for nonlinear waves, the propagation of a solitary wave in a constant water depth of $d=0.30$ m is simulated first. The desired solitary wave height is $H=0.09$ m (the wave height to water depth ratio is $H/d=0.3$). The domains of computations based on Fig. 1 are: $Lc=12$ m, $Hc=0.5$ m, Xp (initial piston position)$=0.5$ m, $Ld1=0.25$ m and $Ld2=2.0$ m. In order to obtain the velocity of the solid object (piston in this case) corresponding to the solitary wave height of H, the Boussinesq solitary wave profile in dimensional quantities was used by Boussinesq (1872):

$$\eta(x,t) = H\,\mathrm{sech}^2 k(x-ct) \tag{15}$$

where H is the solitary wave height; sech( ) is the hyperbolic secant. The wave celerity c and the wave number k are calculated

as:

$$c=\sqrt{g(H+d)} \tag{16}$$

$$k=\sqrt{\frac{3H}{4d^3}} \tag{17}$$

Referring to the solitary wave generation theory developed by Goring (1979), the piston trajectory for generating the solitary waves of all heights is:

$$\frac{\xi(t)}{S}=\tanh 7.6\left(\frac{t}{\tau}-\frac{1}{2}\right) \tag{18}$$

where S is the piston stroke and τ is the duration of motion calculated as:

$$S=\frac{2H}{kd}=\sqrt{\frac{16H}{3d}}d \tag{19}$$

and

$$\tau=\frac{2}{kc}\left(3.80+\frac{H}{d}\right) \tag{20}$$

In the developed model in this study as described above, the velocity of the solid object is set during the computations in each time step. Therefore, the velocity of the piston is calculated by taking derivative of Eq. (18) with respect to time leading to:

$$\frac{V(t)}{S}=\frac{7.6}{\tau}\mathrm{sech}^2 7.6\left(\frac{t}{\tau}-\frac{1}{2}\right) \tag{21}$$

When generating a solitary wave using a piston-type wavemaker, an oscillatory tail is always formed behind the wave. Goring (1979) reported the height of the oscillatory wave to be around 25% of the main wave when using a linear trajectory for the piston movement. The height of the oscillatory wave, however, was reduced to 10% of the main wave when the trajectory of the piston was set based on Eq. (18).

The water free surface profile as the piston moves inside the fluid based on Eq. (18) is depicted in Fig. 4. The time duration and stroke of the piston motion are 3.35 s and 0.379 m, respectively. The generation of the solitary wave is completed in this time after which the shape of the wave remains nearly unchanged. The computational grid size was set based on a mesh refinement study in which the mesh size was progressively increased until no signification changes were observed in the results. For the entire cases in this study, a uniform mesh was used; therefore, the mesh size was characterized by the number of grids used for a length scale considered to be the initial water depth in this case. Three different mesh sizes corresponding to 24, 36 and 48 cells per depth (CPD) in the still water were considered. The solitary wave profiles generated using the three mesh sizes are compared with that of the analytical solution in Fig. 5. A good agreement can be seen between the results of simulations and analytics. The figure also illustrates that the results are independent of the mesh size; as a result, for most simulations in this study, a mesh size of CPD=24 was selected. The discrepancy observed between simulations and analytics at the tail of the solitary wave is due to the existence of the oscillatory wave as described above. The height of this oscillatory wave is about 10% of that of the solitary wave. It should be mentioned that the same procedure taken to obtain the optimum mesh size was also followed for the computational time

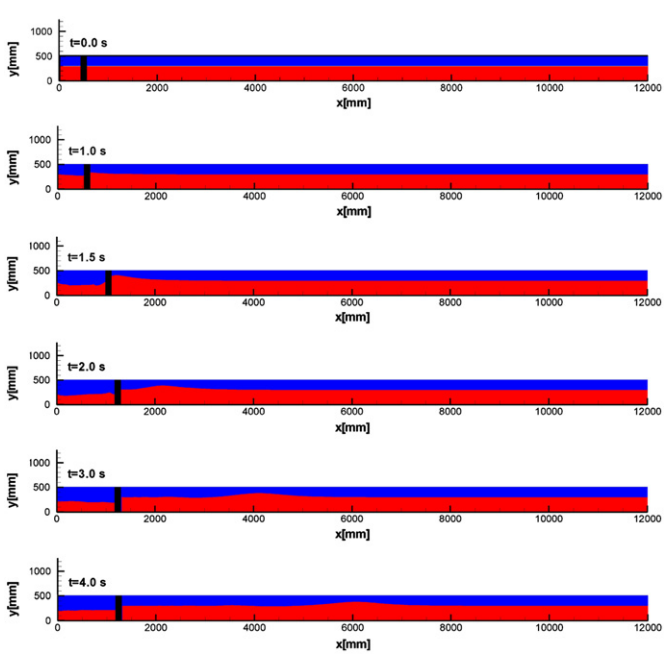

Fig. 4. Evolution of the numerical free surface profile for the solitary wave ($H/d=0.3$).

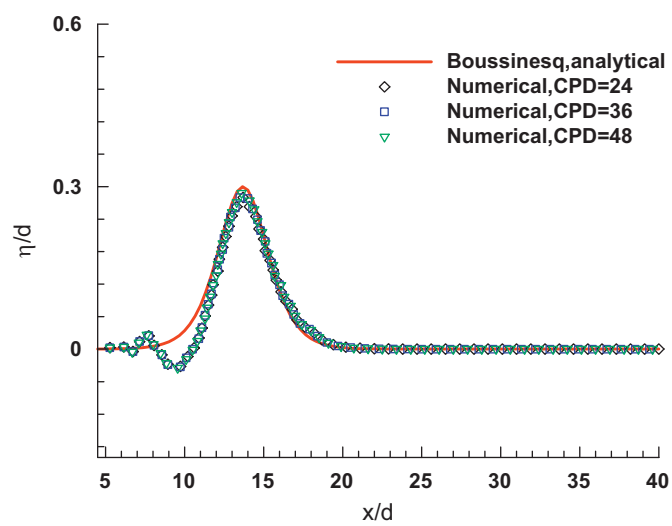

Fig. 5. Free surface profile compared to analytical results for various mesh sizes characterized by CPD (cell-per-depth).

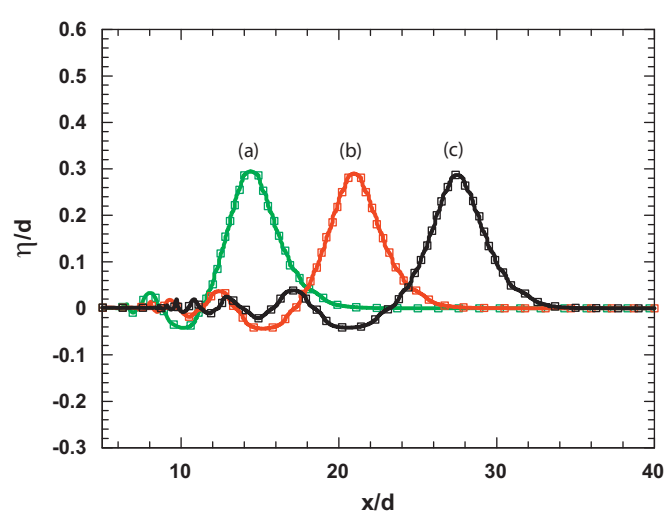

Fig. 6. Numerical free surface profiles at different times: (a) $t_a=3.0$ s; (b) $t_b=4.0$ s; (c) $t_c=5.0$ s.

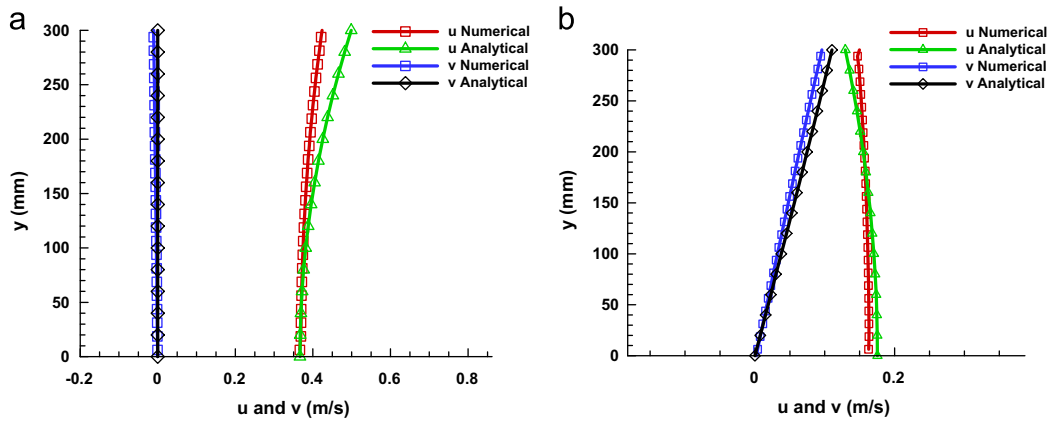

Fig. 7. Horizontal (u) and vertical (v) velocity profiles induced by a solitary wave of $H/d=0.3$.

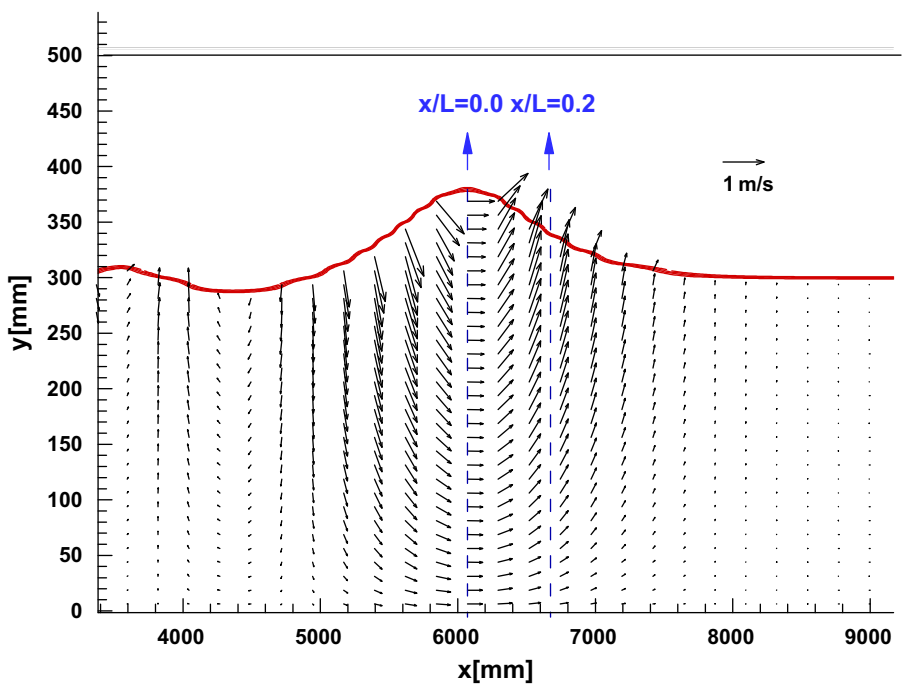

Fig. 8. The solitary wave profile ($H/d=0.3$) and the velocity field at $t=4.0$ s.

step after which a time step of 0.001 s was found to be the optimum value.

The calculated shape of the solitary wave at progressive times is plotted in Fig. 6. The oscillatory tail behind the wave can be well observed in the figure. The wave propagates with a constant velocity and a stable shape towards the end of the computational domain. This is seen in the figure by the equal distances traveled by the wave in the same time intervals.

The accuracy of the numerical results are also validated by comparing the generated velocity field due to wave motion with the analytical results of inviscid fluid (Dean and Dalrymple, 1984). The horizontal and vertical velocity components are plotted in comparison with those of the analytical in Fig. 7 at $t=4$ s elapsed after the start of the piston motion for the solitary wave of $H/d=0.3$. The vertical variation of the velocity components are shown at two positions; just under the wave crest ($x/L=0.0$) and at $0.2L$ after the crest ($x/L=0.2$) (the two positions are also displayed in Fig. 8). A good agreement is seen between the two results; the small discrepancy that exists in the horizontal velocity under the crest may be due to the error in the analytics. The order of accuracy of the analytical solution is $O((H/d)^2, (H/d)(d/L)^2)$ as presented in Dean and Dalrymple (1984). For the solitary wave studied in this paper, $H/d=0.3$ and $d/L=0.0756$, therefore, the accuracy of the analytical solution is in the order of 0.09. Thus, the discrepancy observed between the numerical results and the analytical solution in Fig. 7 may be due to the error in the analytics.

A better representation of the solitary wave profile and the corresponding velocity field at $t=4$ sec are shown in Fig. 8. It is observed that the velocity before the wave crest is downward while after the crest the fluid attains an upward velocity. However, right under the crest the fluid has no vertical velocity.

4.2. Piston type wavemaker – progressive waves

To verify the accuracy of the numerical results in the case of a piston-type wavemaker, the results are compared with reported experiments, analytics and other numerical results. For this purpose, the experimental measurements of Ursell et al. (1960), the second order wavemaker theory of Madsen (1971), and the numerical results of Huang et al. (1998) are considered.

Ursell et al. (1960) performed experiments in a 100-ft-long channel that had an inclined plate with a slope of 1:15 at the far end to absorb the wave energy. The effect of the wave reflection was also taken into account. They divided their experiments into two categories, namely, small wave steepness ($0.002 \le H/L \le 0.03$) and large wave steepness ($0.045 \le H/L \le 0.048$). Most of the experiments (20 cases) were classified as small wave steepness; while the cases with large wave steepness were limited to four cases. Huang et al. (1998) recalculated seven of the 24 experimental cases of Ursell et al. (1960) using their numerical model. In this paper, nine cases including all the four cases of Ursell et al. (1960) with large wave steepness are simulated. A typical case with a higher wave steepness ($H/L=0.06$) is also studied. The experimental conditions corresponding to these cases are shown in Table 1.

In all the numerical simulations, the piston is initially located at $Xp=0.5$ m (Fig. 1a). The piston is placed inside the fluid domain to better visualize the capability of the model to capture the free surface variation as the solid body movies inside the fluid. The domains of computations based on

Fig. 1 are considered as: $Lc > 8L$, $Hc > 1.5d$, $Ld1=0.25$ m and $Ld2 > 2L$. The mesh size considered in this case had 36 cells in the water depth (i.e. CPD=36). Also a time step of $T/100$ (where T is the wave period) is found to be sufficiently small such that the results are independent of time step.

The numerical results for the aforementioned experimental conditions are shown in Fig. 9 in comparison with the experimental and analytical results. To obtain the values of the wave profile from numerical calculations, a section close to the middle of the channel away from the piston and the damping zone at the end of the channel is considered. This section was selected between two positions distanced $5d$ and $25d$ away from the piston location. Specifically, the numerical wave height is calculated by averaging the wave heights from the free surface time history at a fixed position with a distance equal to $15d$ away from the wavemaker initial position. However, the wavelength is calculated by averaging the wave lengths taken from the free surface space distribution inside the selected section.

The numerical results from the present study for both small and large wave steepness are compared with those of the Ursell et al. (1960) experiments and Huang et al. (1998) numerical calculations in Fig. 9. The results from the wavemaker theory are also displayed in the figure. As observed in the figure, the numerical results from the present model agree well with those of the experiments for both small and large wave steepness. Compared to the analytical results, however, it is seen that both numerical simulations and experiments indicate a better agreement in small wave steepness. The time evolution of the numerical free surface profile as the piston starts its motion inside the water for a case with maximum wave steepness (the Case #5 of

Table 1
Piston type wavemaker conditions; *Measured values from Ursell et al. (1960).

Case number	Period (s)	Stroke (cm)	Still water depth (m)	$(H/S)_{theor}$	$(H/S)_{meas*}$	$(H/S)_{num}$	$(2\pi d/L)_{\mathrm{theor}}$	$(2\pi d/L)_{\mathrm{num}}$	$(H/L)_{\mathrm{theory}}$	Experiment number in Ursell et al. (1960)
High wave steepness										
1	0.79	2.54	0.6096	1.99	1.88	1.86	3.98	3.85	0.0488	21
2	0.85	3.15	0.4572	1.85	1.67	1.65	2.55	2.43	0.0485	22
3	0.95	4.50	0.3048	1.39	1.22	1.24	1.51	1.45	0.0439	23
4	0.96	5.73	0.2012	1.05	0.90	0.92	1.09	1.04	0.0409	24
5	1.00	6.40	0.3000	1.30	–	1.10	1.37	1.30	0.0602	–
Small wave steepness										
6	0.92	1.51	0.7315	1.97	1.90	1.98	3.52	3.28	0.0230	9
7	1.11	1.56	0.7315	1.82	1.77	1.70	2.44	2.36	0.0153	13
8	1.27	1.88	0.5090	1.32	1.20	1.28	1.42	1.39	0.0094	17
9	2.09	2.06	0.4785	0.70	0.68	0.73	0.72	0.70	0.0096	15

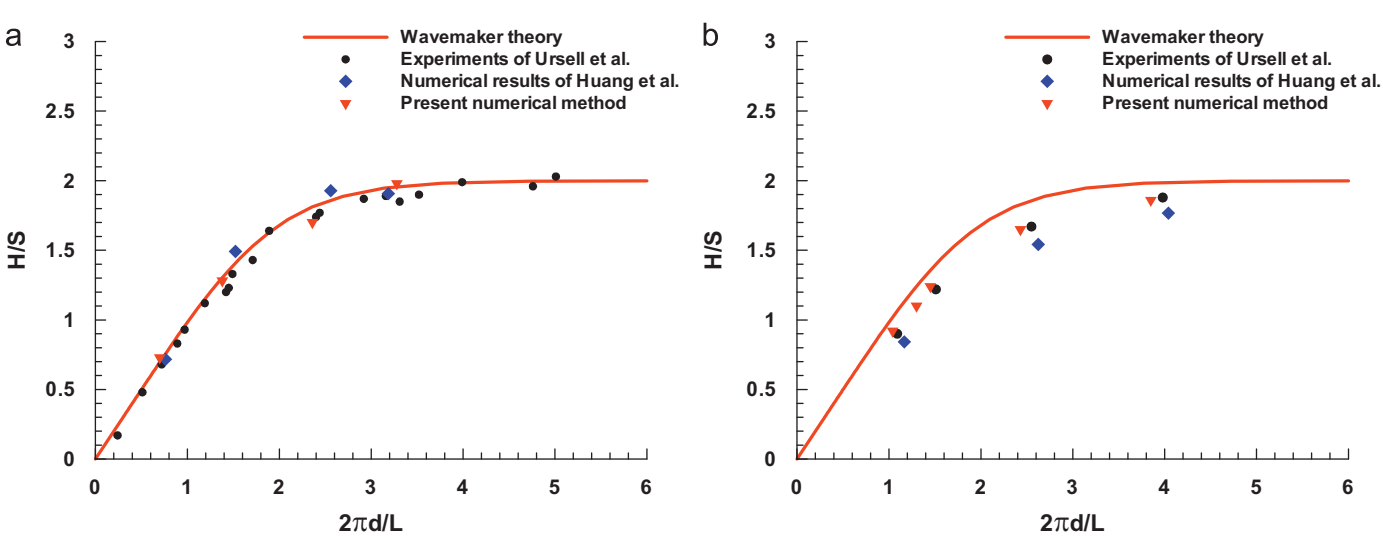

Fig. 9. Comparison between the solution of the wavemaker theory, experiments of Ursell et al. (1960), numerical results of Huang et al. (1998) and the numerical results of the present study.

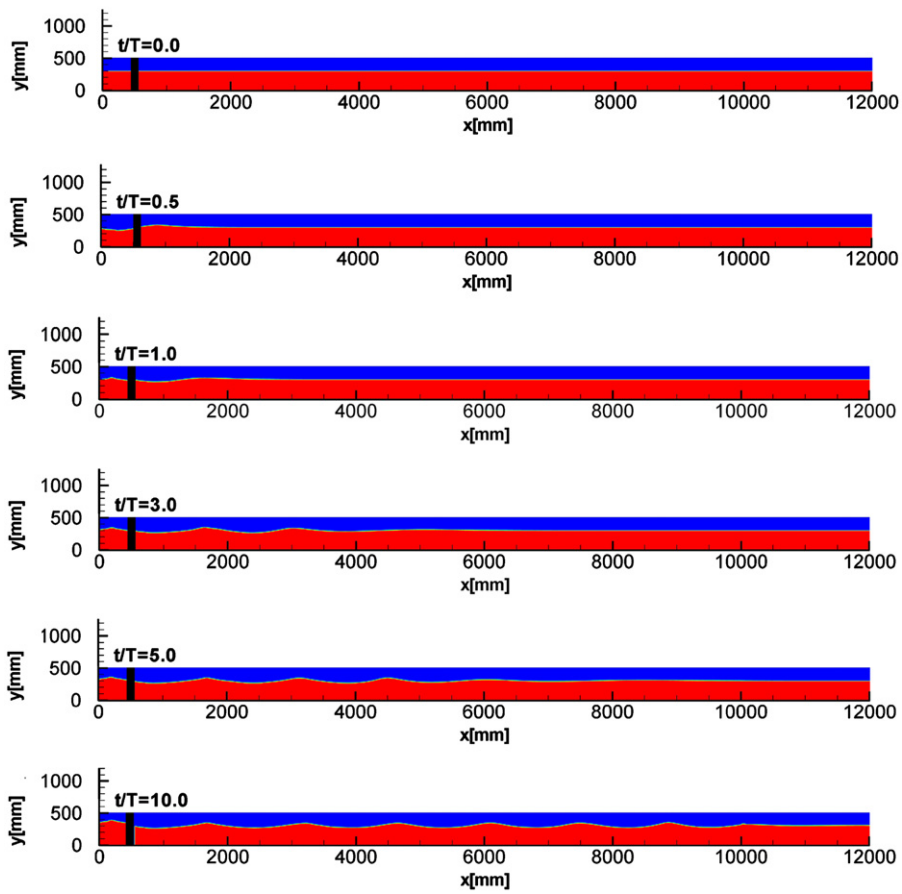

Fig. 10. Evolution of the numerical free surface profile for the piston type wavemaker.

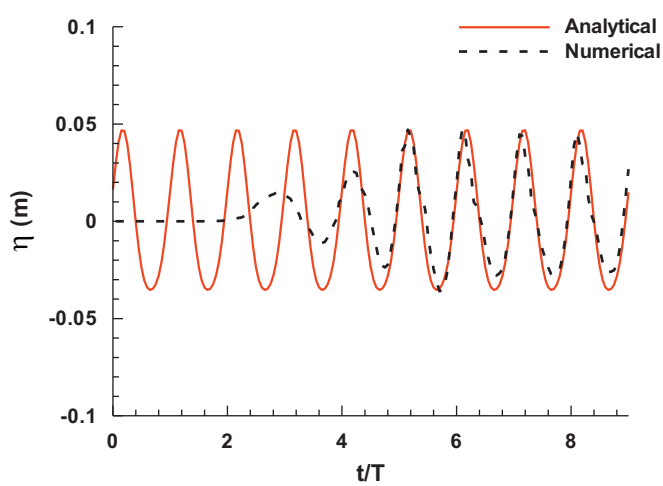

Fig. 11. Comparison between the numerical and analytical free surface elevation at $x=5$ m.

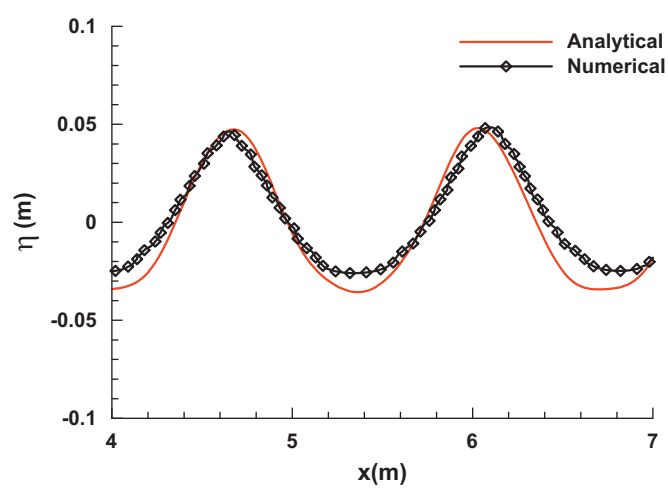

Fig. 12. Comparison between the numerical and analytical wave profile at $t/T=10$.

Table 1) is shown in Fig. 10. It is seen that after nearly $10T$ the wave profile reaches a steady state shape. It should be mentioned that the piston stroke for this case is 6.4 cm (see Table 1) which is too small compared to the channel length (12 m); as a result, the piston displacement cannot be recognized in the figure. Fig. 11 shows time evolution of the numerical water free surface elevation (measured from the still water height) at 15 water depths away from the wavemaker in comparison with the analytical results. After nearly four periods, the wave approaches its steady profile. The numerical and analytical results are also compared with each other at the dimensionless time of $t/T=10.0$ in Fig. 12. The wave profiles from the two results almost coincide in phase but the analytical wave heights are slightly larger than those of the simulations.

4.3. Flap type wavemaker – progressive waves

In the case of flap type wavemaker, the numerical results are compared with the measurements performed in this study as described in Section 3, analytical results as presented in Dean and

Table 2
Flap type wavemaker conditions. *Measured values from the current study.

Case number	Period (sec)	Stroke (cm)	Still water depth (m)	$(H/S)_{theor}$	$(H/S)_{num}$	$(H/S)_{meas*}$	$(2\pi d/L)_{\mathrm{theor}}$	$(2\pi d/L)_{\mathrm{num}}$	$(H/L)_{\mathrm{theor}}$
Small wave steepness									
1	2.1	8.45	0.30	0.28	0.27	0.32	0.548	0.531	0.0069
2	1.40	8.45	0.30	0.46	0.47	0.47	0.875	0.877	0.0180
3	1.05	3.15	0.45	0.93	0.92	—	1.747	1.756	0.0181
4	1.05	2.40	0.8	1.34	1.25	—	2.941	2.717	0.0188
5	1.00	3.00	1.0	1.51	1.40	—	4.030	4.189	0.0291
6	1.40	8.57	0.50	0.65	0.62	0.63	1.222	1.208	0.0217
High wave steepness									
7	0.84	8.47	0.40	1.17	0.96	0.99	2.330	2.244	0.0919
8	1.05	8.45	0.30	0.68	0.65	0.63	1.279	1.160	0.0389
9	0.84	8.45	0.30	0.96	0.76	0.80	1.808	1.804	0.0778
10	1.05	6.30	0.90	1.41	1.25	—	3.299	3.250	0.0518
11	1.05	8.40	1.20	1.55	1.31	—	4.384	4.076	0.0757
12	1.05	4.69	0.67	1.22	1.09	—	2.485	2.392	0.0337

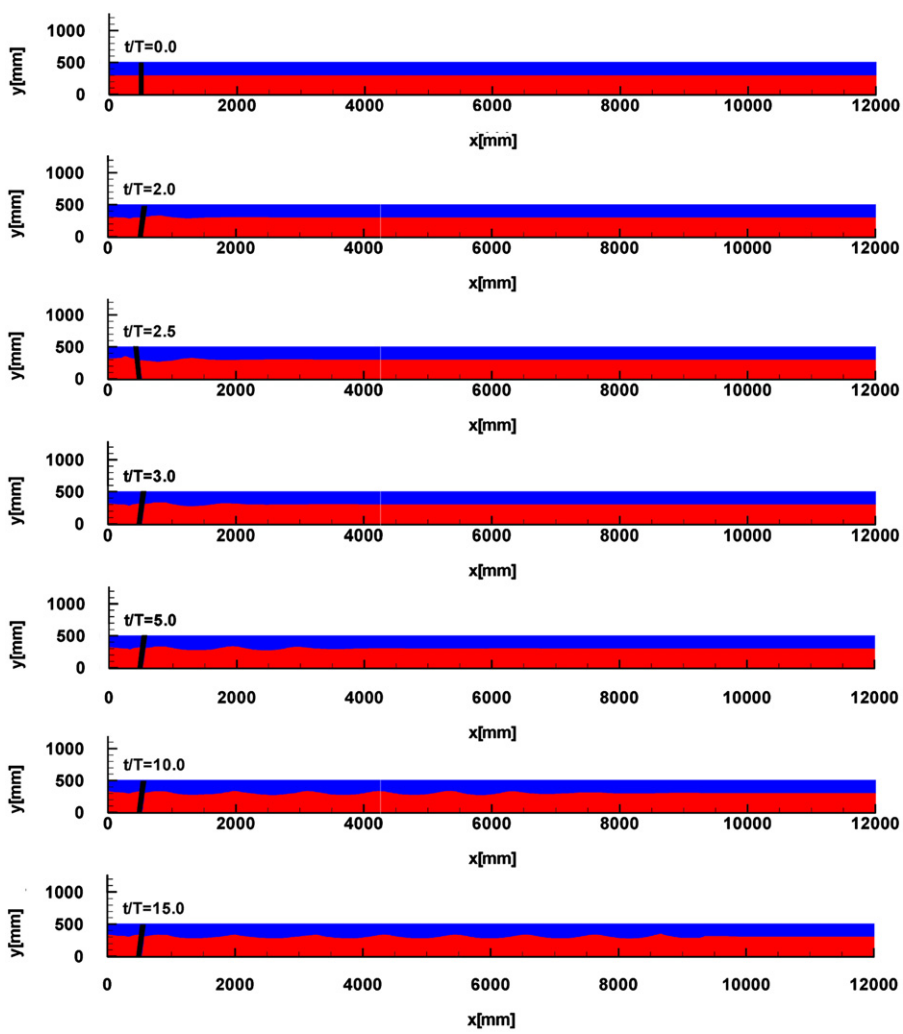

Fig. 13. Evolution of the numerical free surface profile for the flap type wavemaker.

Dalrymple (1984) and the numerical results of the Finnegan and Goggins (2012). Twelve cases are studied in this section, which are again classified as small and large wave steepness including intermediate and deep water, as tabulated in Table 2. However, the experimental results of the present study are limited to intermediate water depths ($\pi/10 \le kd \le \pi$). As a result, for the deep water cases, the numerical results are only compared with the analytical results of the wavemaker theory (Dean and Dalrymple, 1984).

In the numerical simulations, the solid body representing the flapper is initially located at $Xp = 0.5$ m (Fig. 1b). The solid body has no translational velocity, but a simple harmonic angular

velocity as:

$$\theta(t) = \frac{\Delta\theta}{2}\cos\left(\frac{2\pi}{T}t\right) \tag{22}$$

where $\Delta\theta$ is the angular span of the flapper motion. The stroke of the flapper depends on both the angular span and the still water depth as:

$$S = 2d \times \tan\left(\frac{\Delta\theta}{2}\right) \tag{23}$$

For the cases with a high wave steepness and for the deep water cases, the motion of the flapper is initiated using a linear time ramp according to Zhao et al. (2010b). A duration of *2T* for the time ramp was enough to eliminate the initial instabilities.

The time evolution of the numerical free surface profile as the flap starts its motion inside the water for a typical case with relatively large wave steepness (the Case #9 of Table 2) is shown in Fig. 13. The duration of the time ramp used in this case was *2T*. The rotation of the flap and the consequent formation of the progressive waves can be well observed in this figure. The numerical wave heights for all the cases listed in Table 2 are calculated as described for the piston wavemaker, in Section 4.2. The comparison between the numerical results, the wavemaker theory and the experimental data is presented in Fig. 14. In the figure, the ranges of shallow, intermediate and deep water are specified based on the classifications presented by Dean and Dalrymple (1984). For the waves with a small steepness, a good agreement between the numerical and experimental results can be observed especially at intermediate water depths (see Fig. 14a). As observed in the figure, the numerical model of Finnegan and Goggins (2012) fails at deep water waves for a flap-type wavemaker hinged at the bottom of the flume. They found that wave generation in the ANSYS CFX using a flap-type wavemaker is restricted to a low normalized wave number, *kd*. In order to increase this restriction, the hinge of the wavemaker was raised and, with this alteration, it was possible to generate deep water linear waves. This is while the results of the present model do not reveal such a limitation. As seen in Fig. 14a, the model presented in this paper can predict deep water waves with an acceptable accuracy (less than 5%). However, for the cases with a large wave steepness (Fig. 14b) both the numerical and experimental results are about 10% below those of the wavemaker theory; this finding is the same as was observed for the piston type wavemaker (Section 4.2).

The discrepancy between the experiments and the wavemaker theory for the cases with large wave steepness may be attributed to the error in calculating the wave length in the theory. In the wavemaker theory, the wavelength is calculated using the well-known dispersion relation, $\sigma^2 = gk \tanh kd + O(ka)^2$ (Whitham, 1974). This relation shows that as the wave steepness (ka/π) increases, the error in calculating the wave length increases. However, using the proposed method in this paper, one only needs to specify the period and stroke of the wavemaker's trajectory in a water of specific depth. The wave length and the wave height will be calculated through the complete solution of the Navier-Stokes equations. Therefore, the results of the proposed numerical method show a better agreement with the experimental data especially for the waves with high wave steepness.

In order to generate a desired wave, one may use either a piston-type or a flap-type wavemaker by appropriately adjusting the

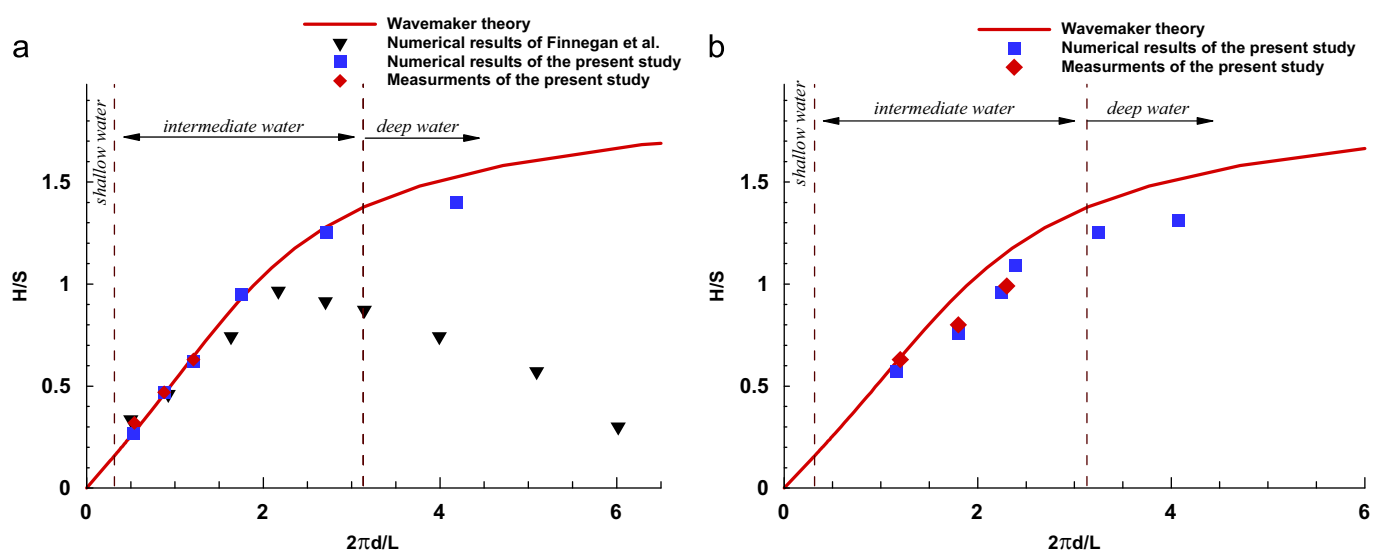

Fig. 14. Comparison between the solution of the wavemaker theory, numerical results of Finnegan and Goggins (2012) and the numerical and experimental results of the present study.

Table 3
Inputs required for the two mavemakers, generating a wave with characteristics of Case #7 of Table 1.

Desired wave characterestics			
Height (cm)	Normalized wave number	Water depth (m)	Period (s)
2.84	2.44	0.7315	1.11
Input required for piston-type wavemaker motion		Input required for flap-type wavemaker motion	
Stroke (cm)	Period (s)	Stroke (cm)	Period (s)
1.56	1.11	1.20	1.11

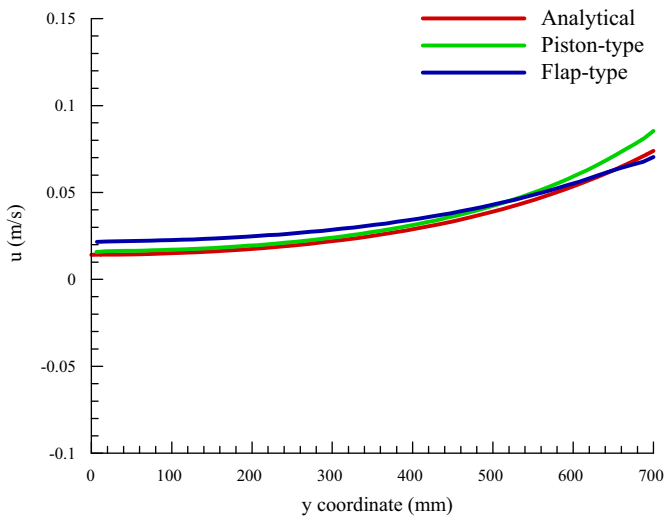

Fig. 15. Comparison between the horizontal velocity profiles beneath a wave generated by a piston-type and a flap-type wavemaker and those of the analytics.

trajectory of the paddle. In shallow water, it is easier to generate the waves with a piston wavemaker motion, as the piston motion more closely resembles the water particle trajectories under the waves, while in deeper water, the flap generator is more efficient (Dean and Dalrymple, 1984). However, far enough from the paddle, no differences are observed between the velocity profiles beneath the waves generated by either of the two wavemakers. The velocity profile beneath a wave far from the wavemaker depends on the wave height, wave period, wave length, and water depth, but not the way the wave has been generated. To examine this fact in this paper, a typical wave with the same characteristics as of Case #7 of Table 1 is considered. The wave is generated by using both the piston-type and the flap-type wavemakers and the results for the velocity under the wave crest are compared. Table 3 provides the wave characteristics and the corresponding required input for each wavemaker. The horizontal velocity profiles under the wave crest at a distance of two wave lengths away from the wavemaker are compared in Fig. 15. The results of the analytical model are also displayed in the figure. The close agreement between the results demonstrates the fact that the velocity profile beneath a wave far from the generating zone does not depend on the generating mechanism.

5. Conclusions

A numerical method is presented in this paper that can simulate the complete physics of the fully nonlinear viscous wave generation phenomenon in both piston and flap-type wavemakers. The prescribed motion of a solid body representing the wave generating mechanism is modeled using the fast fictitious domain method. A variety of linear and nonlinear waves generated by piston and flap-type wavemakers in intermediate and deep waters are simulated using the presented model and the accuracy of the results are verified by a comparison with the results of the wavemaker theory, the available experimental data in the literature, and the experiments preformed in this study. For both the piston and flap-type wavemakers, the numerical results corresponding to the waves with small steepness agree well with the theoretical and experimental results. However, for the cases with large wave steepness, the numerical and experimental wave heights are about 10% lower than those of the analytics. The method presented in this paper can be incorporated in the VOF-type numerical programs for generating fully nonlinear viscous waves used in studying various coastal phenomena in numerical wave tanks.

References

Apsley, D., Hu, W., 2003. CFD simulation of two- and three-dimensional free-surface flow. Int. J. Numer. Method Fluid 42 (5), 465–491.
Borgman, L.E., Chappelear, J.E., 1958. The Use of the Stokes-Struik Approximation for Waves of Finite Height. In: Proceedings of the 6th Conference Coastal Eng., ASCE, Council on Wave Research, Berkeley, California.
Boussinesq, J., 1872. Theorie des Ondes et des Remous qui se Propagent le Long d'un Canal Rectangulaire Horizontal, en Communiquant au Liquide Contenu dans ce Canal de Vitesses Sensiblement Parreilles de la Surface au Fond. J. Math. Pure Appl. 17, 55–108 2nd Series.
Brorsen, M., Larsen, J., 1987. Source generation of nonlinear gravity waves with the boundary integral equation method. Coast. Eng. 11 (2), 93–113.
Chan, R.K.C., Street, R.L., 1970. A computer study of finite-amplitude water waves. J. Comput. Phys. 6 (1), 68–94.
Chaplin, J.R., 1979. Developments of stream-function wave theory. Coast. Eng. 3 (0), 179–205.
Chappelear, J.E., 1961. Direct numerical calculation of nonlinear ocean waves. J. Geophys. Res. 66 (2), 501–508.
Dean, R.G., 1965. Stream function representation of non-linear ocean waves. J. Geophys. Res. 70 (18), 4561–4572.
Dean, R.G., Dalrymple, R.A., 1984. Water Wave Mechanics for Engineers and Scientists. World Scientific Publishing Co. Re. ttd., Singapore.
Dong, C.M., Huang, C.J., 2004. Generation and propagation of water waves in a two-dimensional numerical viscous wave flume. J. Waterway, Port, Coastal, .Ocean Eng. 130 (3), 143–153.
Fenton, J.D., 1985. A fifth-order Stokes theory for steady waves. J. Waterway Port Coastal Ocean Eng. 111 (2), 216–234.
Fenton, J.D., 1988. The numerical solution of steady water wave problems. Comput. Geosci. 14 (3), 357–368.
Finnegan, W., Goggins, J., 2012. Numerical simulation of linear water waves and wave–structure interaction. Ocean Eng. 43 (0), 23–31.
Flick, R.E., Guza, R.T., 1980. Paddle Generated Waves in Laboratory Channels. J. Waterway Port Coastal .Ocean Div. 106 (1), 79–97.
Goring, D.G., 1979. Tsunamis-the propagation of long waves onto a shelf, W.M. Keck Laboratory of Hydraulics and Water Resources, California Institute of Technology, Pasadena, California, California.
Hafsia, Z., Hadj, M.B., Lamloumi, H., Maalel, K., 2009. Internal inlet for wave generation and absorption treatment. Coast Eng. 56 (9), 951–959.
Harlow, F.H., Amsden, A.A., 1971. Fluid Dynamics: A LASL Monograph, Mathematical solutions for problems in fluid dynamics. Los Alamos Scientific Laboratory Report LA 4700.
Harlow, F.H., Welch, J.E., 1965. Numerical calculation of time-dependent viscous incompressible flow of fluid with free surface. Phys. Fluids 8, 2182–2189.
Havelock, T.H., 1929. Forced Surface Wave on Water. Philos. Mag. 8 (7), 569–576.
Hieu, P.D., Tanimoto, K., 2006. Verification of a VOF-based two-phase flow model for wave breaking and wave-structure interactions. Ocean Eng. 33 (11–12), 1565–1588.
Hirt, C.W., Nichols, B.D., 1981. Volume of fluid (VOF) method for the dynamics of free boundaries. J. Comput. Phys. 39 (1), 201–225.
Huang, C.J., Dong, C.M., 2001. On the interaction of a solitary wave and a submerged dike. Coast Eng. 43, 265–286.
Huang, C.J., Zhang, E.C., Lee, J.F., 1998. Numerical simulation of nonlinear viscous wavefields generated by piston-type wavemaker. J. Eng. Mech. 124 (10), 1110–1120.
Hur, D.S., Mizutani, N., 2003. Numerical estimation of the wave forces acting on a three-dimensional body on submerged breakwater. Coast. Eng. 47 (3), 329–345.
Hur, D.S., Mizutani, N., Kim, D.S., 2004. Direct 3-D numerical simulation of wave forces on asymmetric structures. Coast Eng. 51 (5–6), 407–420.
Hyun, J.M., 1976. Theory for hinged wavemakers of finite draft in water of constant depth. J. Hydronaut. 10 (1), 2–7.
Karim, M.F., Tanimoto, K., Hieu, P.D., 2009. Modelling and simulation of wave transformation in porous structures using VOF based two-phase flow model. Appl. Math. Model. 33 (1), 343–360.
Kawasaki, K., 1999. Numerical simulation of breaking and post-breaking wave deformation process around a submerged breakwater. Coast Eng. 41, 201–223.
Kershaw, D.S., 1978. The incomplete Cholesky-conjugate gradient method for the iterative solution of systems of linear equations. J. Comput. Phys. 26 (1), 43–65.
Larsen, J., Dancy, H., 1983. Open boundaries in short wave simulations—a new approach. Coast Eng. 7 (3), 285–297.
Li, B., Fleming, C.A., 2001. Three -dimensional model of Navier–Stokes equations for water waves. J. Waterway, Port, Coastal Ocean Eng. 127 (1), 16–25.
Li, Y.S., Liu, S.X., Yu, Y.X., Lai, G.Z., 1999. Numerical modeling of Boussinesq equations by finite element method. Coast Eng. 37 (2), 97–122.
Lin, P., Liu, P.L.F., 1999. Internal wave-maker for Navier-Stokes equations models. J. Waterway, Port, Coastal, Ocean Eng. 125 (4), 207–215.
Lin, P., Liu, P.L.F., 1998. A numerical study of breaking waves in the surf zone. J Fluid Mech. 359, 239–264.
Lin, P., Liu, P.L.F., 2004. Discussion of "Vertical variation of the flow across the surf zone" [Coast. Eng. 45 (2002) 169–198]. Coast Eng. 50 (3), 161–164.

Liu, S.X., Teng, B., Yu, Y.X., 2005. Wave generation in a computation domain. Appl. Math. Model. 29 (1), 1–17.
Madsen, O.S., 1971. On the Generation of Long Waves. J. Geophys. Res. 76, 8672–8683.
Mirzaii, I., Passandideh-Fard, M., 2012. Modeling free surface flows in presence of an arbitrary moving object. Int. J. Multiphase Flow 39 (0), 216–226.
Moubayed, W., Williams, A., 1993. Second-order bichroamatic waves produced by a generic planar wavemaker in a two-dimensional flume. J. Fluid Struct. 8 (73–92), 73.
Park, J.C., Kim, M.H., Miyata, H., Chun, H.H., 2003. Fully nonlinear numerical wave tank (NWT) simulations and wave run-up prediction around 3-D structures. Ocean Eng. 30 (15), 1969–1996.
Schäffer, H.A., 1996. Second-order wavemaker theory for irregular waves. Ocean Eng. 23 (1), 47–88.
Schwartz, L.W., 1974. Computer extension and analytic continuation of Stokes' expansion for gravity waves. J. Fluid Mech. 62 (03), 553–578.
Sharma, N., Patankar, N.A., 2005. A fast computation technique for the direct numerical simulation of rigid particulate flows. J. Comput. Phys. 205, 439–457.
Shen, L., Chan, E.-S., 2008. Numerical simulation of fluid–structure interaction using a combined volume of fluid and immersed boundary method. Ocean Eng. 35 (8-9), 939–952.
Suea, Y.C., Chernb, M.J., Hwanga, R.R., 2005. Interaction of nonlinear progressive viscous waves with a submerged obstacle. Ocean Eng. 32, 893–923.
Tang, C.T., Patel, V.C., Landweber, L., 1990. Viscous effects on propagation and reflection of solitary waves in shallow channels. J. Comput. Phys. 88 (1), 86–113.
Troch, P., De Rouck, J., 1999. An active wave generating-absorbing boundary condition for VOF type numerical model. Coast Eng. 38 (4), 223–247.
Ursell, F., Dean, R.G., Yu, Y.S., 1960. Forced small-amplitude water waves: A comparison of theory and experiment. J. Fluid Mech. 7, 32–53.
Wang, H.W., Huang, C.J., Wu, J., 2007. Simulation of a 3D Numerical Viscous Wave Tank. J. Eng. Mech. 133 (7), 761–772.
Wei, G., Kirby, J.T., Sinha, A., 1999. Generation of waves in Boussinesq models using a source function method. Coast Eng. 36 (4), 271–299.
Whitham, G.B., 1974. Linear and Nonlinear Waves. Wiley, New York.
Wood, D.J., Pedersen, G.K., Jensen, A., 2003. Modelling of run up of steep non-breaking waves. Ocean Eng. 30 (5), 625–644.
Youngs, D.L., 1984. An interface tracking method for a 3D Eulerian hydrodynamics code. Technical Report 44/92/35, AWRE.
Zhang, H., Schäffer, H.A., 2007. Approximate stream function wavemaker theory for highly non-linear waves in wave flumes. Ocean Eng. 34 (8-9), 1290–1302.
Zhao, X.Z., Hu, C.H., Sun, Z.C., 2010a. Numerical simulation of extreme wave generation using VOF method. J. Hydrodyn. Ser. B 22 (4), 466–477.
Zhao, X.Z., Hu, C.H., Sun, Z.C., Liang, S.X., 2010b. Validation of the initialization of a numerical wave flume using a time ramp. Fluid Dyn. Res. 42, 045504.